Ambient pressure CO₂ hydrogenation over a cobalt/manganese-oxide nanostructured interface: A combined in situ and ex situ study

Gábor Varga [a,b,1], András Sápi [b,1,*], Tamás Varga [b], Kornélia Baán [b], Imre Szenti [b], Gyula Halasi [c], Róbert Mucsi [b], László Óvári [c,d], János Kiss [b,d], Zsolt Fogarassy [e], Béla Pécz [e], Ákos Kukovecz [b], Zoltán Kónya [b,d]

[a] Materials and Solution Structure Research Group, Institute of Chemistry, University of Szeged, Aradi Vértanúk tere 1, Szeged H-6720 Hungary
[b] University of Szeged, Interdisciplinary Excellence Centre, Department of Applied and Environmental Chemistry, H-6720, Rerrich Béla tér 1, Szeged, Hungary
[c] Extreme Light Infrastructure-ALPS, ELI-HU Non-profit Ltd., Dugonics tér 13, Szeged H-6720 Hungary
[d] MTA-SZTE Reaction Kinetics and Surface Chemistry Research Group, Rerrich Béla tér 1, Szeged H-6720, Hungary
[e] Institute for Technical Physics and Materials Science, Centre for Energy Research, Hungarian Academy of Sciences, Konkoly-Thege M. út 29-33, 1121 Budapest, Hungary

ARTICLE INFO

ABSTRACT

We report on a cobalt/manganese-oxide interface catalyst with outstanding activity and selectivity towards methane even at high temperatures and ambient pressure in CO_2 hydrogenation. The catalyst was formed from a $MnCo_2O_4$-based spinel structure during the oxidative-reductive pretreatment process just before the catalytic tests. Several Mn-, Fe- and Ni-containing cobaltite spinel and reverse spinel structures were tested to find the best overall performer. The reusable $MnCo_2O_4$-based structure featured a CO_2 consumption rate of ~8500 nmol*g⁻¹*s⁻¹. Even though methane is not the thermodynamically favoured product, it was produced with ~80% and ~50% selectivity at ambient pressure at 673 K and 823 K, respectively. This unexpected finding is linked to the presence of a unique nanostructured Co/Mn(II)O catalyst with a surface composition of $Mn_{3.3}Co_{2.0}O_{4.7}$ formed after the pretreatment activation step. Over this phase, the reduction of CO_2 progresses through bridge bonded formate located at the Co/Mn²⁺ interface and this is mostly responsible for high temperature methane formation. This hypothesis is proven here by the reported combination of ex-situ XRD, TPR, HRTEM-ED, HAADF-EDX and in-situ NAP-XPS and DRIFTS techniques.

© 2020 The Authors. Published by Elsevier Inc. This is an open access article under the CC BY-NC-ND license (http://creativecommons.org/licenses/by-nc-nd/4.0/).

1. Introduction

CO₂ is a problem and there is a need for chemical activation of such stable molecule [1,2]. High pressure techniques can lead to methanol [3] and other high energy fuels [4], however, producing high-energy-containing products at ambient pressures is challenging. Beside methanol and C₂<-fuel synthesis at higher pressures [5–7], ambient pressure thermally activated techniques for CO₂ hydrogenation usually produce carbon-monoxide and methane [8–15]. One of the industrial techniques is the combined Power-to-gas (PtG) technology, where chemical energy carriers are built upon the peak power production period of the electricity production. PtG involves the production of hydrogen by water electrolysis and the methanation (Sabatier reaction) between H₂ and CO₂ to produce synthetic natural gas (SNG) [16]. The produced SNG is easy to store and can be transported in existing natural gas pipelines. Here we present an unusual, noble-metal free Cobalt/Manganese-oxide catalysts which evolves from a special cobalt-spinel structure during the catalyst activation having a high methane selectivity even if at high temperature and ambient pressure. We believe that the Co/MnOx structure is new and also can be promising for the future CO₂ activation chemistry as we found only a very recent paper about producing liquid fuels by using Co₆/MnOx catalyst [6]. On the other hand, the usage of solid solution structures for CO₂ hydrogenation is still very new and promising [17].

Having outstanding hydrocracking behaviour, noble-metal-containing systems have been efficiently applied as catalysts for CO₂ activation [18]. However, because of environmental and economic reasons, there is an increasing demand for noble-metal-free transition metal catalysts [19]. Similarly to Fisher-Tropsch synthesis, cobalt- and iron-containing systems proved to be suitable catalysts in hydrocracking [5,20,21]. Furthermore, both the catalytic activity and CH₄-selectivity of these systems increased by doping them with other metal ions [22–24]. Nickel, copper

and manganese ions could positively influence the reaction pathways by creating new reaction routes (at high pressure) [25–27].

As noble metals and transition metal-containing mixed oxides and cobaltites have been efficiently used to catalyse CO_2 hydrogenation. This paper is focusing on the usage of a special nanoparticle/oxide interface structure evolved from different Mn-, Fe- and Ni-containing cobaltite spinel and reverse spinel structures. The highly active (CO_2 consumption rate = ~8500 nmol*g^{-1}*s^{-1}) $MnCo_2O_4$-based structure was producing methane with ~50% selectivity at ambient pressure at 823 K, where the reason of the outstanding methane selectivity is the presence of a special nanostructured Co/Mn(II)O catalyst where the CO_2 reaction route is favoured through the formate pathway towards methane as evidenced by ex-situ HR-TEM-EDX, in-situ NAP-XPS as well as in-situ DRIFTS techniques.

2. Experimental part

2.1. Materials

All the AR-chemical reagents were purchased from Merck and Sigma-Aldrich and used as received without further purification.

2.2. Synthesis

The spinel-based catalysts were prepared by the thermal decomposition of the precursor mixed hydroxides described by Yamamoto et al. [28]. Stoichiometric aqueous solutions of cobalt nitrate ($Co(NO_3)_2 \cdot 6H_2O$; c_1 = 0.29 M, c_2 = 0.26 M; c_3 = 0.2 M) and other transition metal nitrates ($Ni(NO_3)_2 \cdot 6H_2O$ or $Fe(NO_3)_3 \cdot 9H_2O$ or $Mn(NO_3)_2 \times 4 H_2O$; c_1 = 0.01 M; c_2 = 0.04 M; c_3 = 0.1 M) were mixed and 1 M NaOH was added dropwise under bubbling Ar to avoid carbonation. The precipitate was separated by centrifugation, washed with hot (333 K) distilled water, and dried at 403 K for 24 h. The thus obtained solid was heated in air at 573 K for 2 h which was followed by composition-dependent dehydration (T_{Ni} = 823 K; T_{Mn} = 873 K; T_{Fe} = 923 K) on air for 8 h.

2.3. Characterization

X-ray Diffraction (XRD) patterns were recorded on a Rigaku XRD-MiniFlex II instrument applying Cu Kα radiation (λ = 0.15418 nm), 40 kV accelerating voltage at 30 mA.

The morphology of the freshly prepared and used samples was studied by scanning electron microscopy (SEM). The SEM images were registered on an S-4700 scanning electron microscope (SEM, Hitachi, Japan) with accelerating voltage of 10–18 kV.

More detailed images, both on the freshly prepared and the used samples, were captured by transmission electron microscopy (TEM), and information on the crystal structures was gathered by selected area diffraction (SAED). For these measurements, a FEI Tecnai[TM] G2 20 X-Twin type instrument operated at an acceleration voltage of 200 kV, a Philips CM20 instrument running at an acceleration voltage of 200 kV and a Cs-corrected (S)TEM of Themis instrument were used. The TEM-EDS mapping was monitored by Super-X detectors of the Themis instrument at 200 kV. SAED patterns were recorded and evaluated by using of the ProcessDiffraction software [29–31].

The specific surface area of the samples was determined by the Brunauer-Emmett-Teller (BET) method (adsorption of N_2 at 77 K). For these measurements, a NOVA3000 instrument was applied (Quantachrome, USA). The samples were flushed with N_2 at 373 K for 5 h to clean the surface of any adsorbents.

Raman spectra were recorded with a Thermo Scientific[TM] DXR[TM] Raman microscope at an excitation wavelength of 635 nm applying 10 mW laser power and averaging 20 spectra with an exposition time of 6 s.

Temperature-programmed reduction (TPR) was performed in a BELCAT-A apparatus using a reactor (quartz tube with 9 mm outer diameter) that was externally heated. Before the measurements, the catalyst samples were treated in oxygen at 573 K for 30 min. Thereafter, the samples were cooled in flowing Ar to room temperature and equilibrated for 15 min. The oxidized samples were flushed with Ar containing 10% H_2, the reactor was heated linearly at a rate of 20 K/min up to 1373 K and the H_2 consumption was detected by a thermal conductivity detector (TCD).

Infrared spectroscopy measurements (In-situ Diffuse Reflectance Infrared Fourier Transform Spectroscopy (DRIFTS)) were carried out with an 'Agilent Cary-670' FTIR spectrometer equipped with 'Harrick Praying Mantis' diffuse reflectance attachment. The sample holder had two BaF_2 windows in the infrared beampath. The spectrometer was purged with dry nitrogen. The spectrum of the pre-treated catalyst was used as background. At room temperature, the mixture of CO_2:H_2 (molar ratio of 1:4) was introduced into the DRIFTS cell. The tubes were externally heated to avoid condensation. The catalyst was heated under the reaction feed linearly from room temperature to 773 K, with a heating rate of 20 K*min^{-1} and IR spectra were measured at 50 K intervals. All spectra were recorded between 4000 and 800 cm^{-1} at a resolution of 2 cm^{-1}. Typically, 32 scans were registered. Due to the short optical path within the DRIFTS cell, the contribution of the reactant gases was negligibly small, and from gas phase products only the most intense features were observable.

Near ambient pressure X-ray photoelectron spectroscopy (NAP-XPS) measurement were carried out using the SPECS system of the Charles University, Prague. A monochromatic Al Kα X-ray source was used for excitation, and a PHOIBOS 150 Hemispherical Energy Analyser coupled with a differentially pumped electrostatic pre-lens system was used for spectrum collection. Spectra presented were obtained with a constant pass energy of 20 eV. The in-situ parameters were performed with the same parameters as mentioned above using a total pressure of 5 mbar.

2.4. Hydrogenation of carbon-dioxide in a continuous flow reactor

Before the catalytic experiments (both in continuous-flow reactor and in ambient pressure XPS chamber) the catalysts were oxidized in O_2 atmosphere at 573 K for 30 min and thereafter were reduced in H_2 at 573 K for 60 min to create the active form of catalysts.

The catalytic reactions were performed in a fixed-bed continuous-flow reactor (200 mm long with 8 mm i.d.), which was heated externally. The dead volume of the reactor was filled with quartz beads. The operating temperature was controlled by a thermocouple placed inside the oven close to the reactor wall, to assure precise temperature measurement. For catalytic studies, small fragments (about 200–500 μm, but no bigger than 1 mm) of slightly compressed pellets were used. Typically, the reactor filling contained 150 mg catalyst. In the reacting gas mixture, the CO_2:H_2 molar ratio was 1:4, if not denoted otherwise. The CO_2:H_2 mixture was introduced with the aid of mass flow controllers (Aalborg), the total flow rate was 50 ml/min. The reacting gas flow entered and left the reactor through an externally heated tube in order to avoid condensation of the products. The analysis of the products and reactants was performed with an Agilent 4890 gas chromatograph using a Porapak QS packed column which was connected to the TCD and an Equity-1 column was connected to the FID (flame ionization detector).

3. Results and discussion

Cobaltite-based spinel structures were synthesized by a hydrothermal method using different ratio of Fe, Ni and Mn to achieve a mixed oxide spinel structures.

For $Mn_xCo_{3-x}O_4$, several well-defined diffraction peaks are observed at 2θ values of 31.2°, 36.8°, 38.8°, 44.6°, and 59.9°, corresponding to the (2 2 0), (3 1 1), (2 2 2), (4 0 0), and (5 1 1) planes of cubic $Mn_xCo_{3-x}O_4$ structure as identified by JCPDS database, respectively (PDF#23-1237) (Fig. S1) [50]. The diffraction peaks of $Ni_xCo_{3-x}O_4$ are slightly shifted to lower 2θ compared to those of $Mn_xCo_{3-x}O_4$, indicating a slight increment in the unit cell size due to the substitution of Mn to Ni. For $Ni_xCo_{3-x}O_4$, the characteristic peaks at 31.1°, 36.4°, 38.4°, 44.3°, and 58.8° 2θ values can be assigned to (2 2 0), (3 1 1), (2 2 2), (4 0 0), and (5 1 1) crystal planes, respectively (PDF#02-1074) [51]. These diffraction peaks indicate the presence of spinel nanocrystallites (PDF#75-0035) [52]. The diffractions of iron-containing and pure Co_3O_4 systems give rise to the same peaks as Ni-containing systems and those were indexed in accordance with spinel phases, revealing a well-crystallized cubic spinel-type phase (JCPDS # 02-1073).

Micro-Raman spectra of the $Mn_xCo_{3-x}O_4$, $Ni_xCo_{3-x}O_4$ and $Fe_xCo_{3-x}O_4$ samples recorded using 635 nm excitation are shown in Fig. 1. The five Raman lines observed in the spectra at around 690, 610, 510, 480, and 190 cm^{-1} are assigned as A_g^1; F_{2g}^2; F_{2g}^1; E_g and T_{2g} modes, respectively [32]. The Raman peaks in the region of 660–720 cm^{-1} reflect the nature of the tetrahedra in cobaltites, while those in the 460–640 cm^{-1} region reflect the nature of the octahedra [33]. The shifting of the peak at around 480 cm^{-1} in the spectrum of $Fe_xCo_{3-x}O_4$ may be attributed to the high degree of disorder at the octahedral sites due to the shifting of iron ions from octahedral sites to tetrahedral sites [34]. Both XRD and Raman measurements confirm that a mixed spinel oxide structure was successfully synthesized in case of the iron-containing system. Significant differences in the Raman peaks of $Ni_xCo_{3-x}O_4$ and $Mn_xCo_{3-x}O_4$ compositions could not be observed compared to the peaks of pure cobaltite, indicating the formation of inverse spinel system.

It is interesting to note, that the ratio of the metal ion (Fe, Mn, Ni) and cobalt ion in the spinel samples has a significant effect on the structure on both the micro- and the mesoscale. SEM images showed that spinels with a fraction ratio metal ion: cobalt ion formula (i. e. $Me_{0.4}Co_{2.6}O_4$, $Me_{0.1}Co_{2.9}O_4$) have irregular cauliflower-like structure in the mesoscale, while the $MeCo_2O_4$ mixed oxide and the pure cobaltite structure exhibit semi-regular, rounded cubic shape morphology (Fig. S2). Similar phenomena were found in the research of layered double hydroxide (LDH) structure with $MeCo_2O_4$ compositions [35,36,37]. SEM-EDX measurements provided semi-quantitative information about the composition of the catalysts and these data are in accordance with the initial concentration ratio, thus confirming the resulted spinel structures (Table S1).

On the other hand, TEM images showed that in the case of spinels with a fraction ratio metal ion: cobalt ion formula (i. e. $Me_{0.4}Co_{2.6}O_4$, $Me_{0.1}Co_{2.9}O_4$) the particle size was between 50 and 500 nm (Fig. 2). However, in the case of the $MeCo_2O_4$ mixed oxide and the pure cobaltite structure, a more porous primary and secondary structure was observed in the micropore regime, which correlates well with the high surface area, (90–110 m^2/g, 2–3 times higher values compared to other catalysts) of these catalysts (Table S1). As XRD calculation showed, the primary grains with an average size of ~20 nm were aggregated into bigger clusters.

3.1. Hydrogenation of CO_2 over cobaltites

Ni, Fe and Mn-containing cobaltites and Co_3O_4 spinel as reference were tested in CO_2 hydrogenation to form carbon-monoxide, methane, and ethene at 573–823 K in a fix bed flow catalytic reactor at ambient pressure. The summarized catalytic activity results, demonstrated by consumption rates and conversions, and collected on Figs. 3 and S3, respectively.

In the case of the reaction tested at 573 K, the pure cobalt-spinel was proven to be active (1410 nmol*g^{-1}*s^{-1}), as well as the iron-containing systems, except for the $Fe_{0.1}Co_{2.9}O_4$ composition. The manganese-cobaltites are more than 2 times more active compared to the Co_3O_4 at this temperature. The nickel-spinels did not exhibit considerable activity. In the presence of pure and manganese-containing cobaltites, the formation rate increased appreciably by increasing the temperature to 673 K, and the $MnCo_2O_4$ solid solution had the highest activity among these cata-
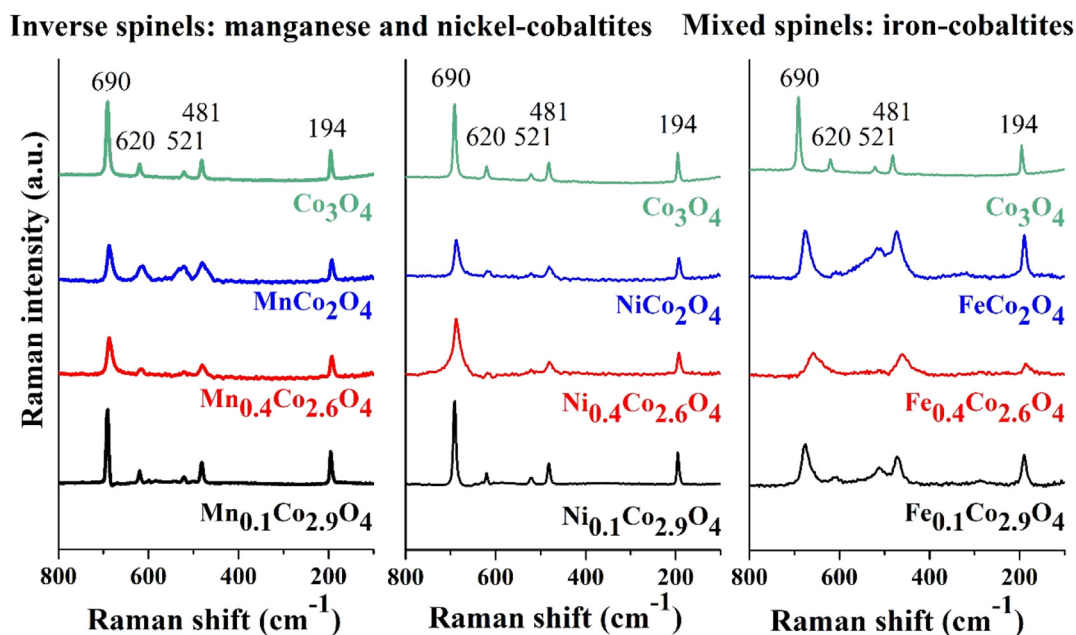
Inverse spinels: manganese and nickel-cobaltites   Mixed spinels: iron-cobaltites

Fig. 1. Raman spectra of $Mn_xCo_{3-x}O_4$, $Ni_xCo_{3-x}O_4$ and $Fe_xCo_{3-x}O_4$ showing the presence of inverse spinel as well as mixed oxide spinel structure in the case of manganese- and nickel cobaltite as well as iron-cobaltite, respectively.
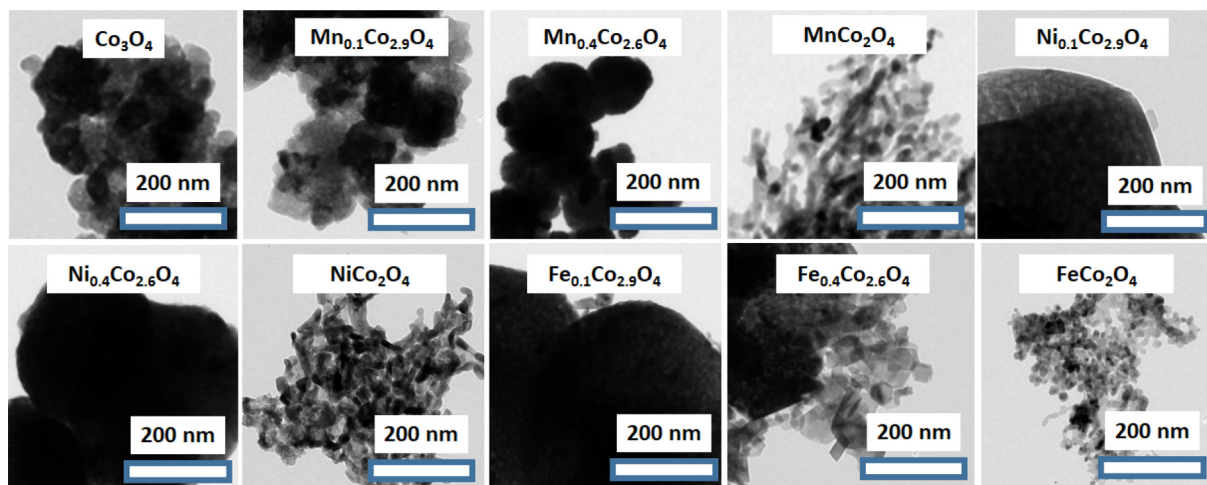
Fig. 2. TEM images of the as-synthetized spinel structures.

lysts (5100 $nmol^*g^{-1*}s^{-1}$). Furthermore, this activity of the manganese-based catalysts is superior to those reported in the literature (Table S2). The activity of the iron-containing systems approached 3500 $nmol^*g^{-1*}s^{-1}$ (that of the Co_3O_4), in addition, the nickel-spinels showed higher activity compared to the pure cobaltites in case of $NiCo_2O_4$ and $Ni_{0.4}Co_{2.6}O_4$. Furthermore, all modified cobaltites were more active than the pure spinel at 823 K. The highest activity (~8500 $nmol^*g^{-1*}s^{-1}$) was achieved using the $MnCo_2O_4$ catalysts at 823 K, which can be denoted as an outstanding performance compared to the results from earlier studies (Table S2). Some of the catalysts mentioned in Table S2. presented higher activity towards methane in CO_2 activation than our $MnCoO_4$ catalysts at 400 °C [38,39], however, those catalysts are losing CH_4-selectivity rapidly at higher temperature while Mn-based cobaltite spinel structure still has significant CH_4-selectivity even at 873 K.

The superior activity was slightly reduced after regeneration of the catalysts at 873 K (oxidation by O_2 followed by 573 K reduction with H_2 conditions for two consecutive tests) (Fig. S4), where the restitution of the pristine $MnCoO_4$ crystal structure was evidenced by XRD (Fig. S5).

Not only the activity of the cobaltite was influenced by the incorporation of transition metals, but also its selectivity (Fig. 4). The pure cobaltite had 92% selectivity for methane at 573 K. However, 60% methane selectivity was detected at 673 K and only CO was formed at 823 K. On the contrary, one of both the manganese-, and iron-containing systems demonstrated 100% methane selectivity at 573 K, moreover, up to 90% methane selectivity was observed in case of $Fe_{0.1}Co_{2.9}O_4$ even at 673 K. Furthermore, all modified spinels produced measurable amounts of methane at 823 K. The $MnCo_2O_4$ structure exhibited ~50% methane selectivity at ambient pressure and at 823 K. Table S2 shows that this ambient pressure and high temperature methane selectivity is outstanding compared to other noble metal-free or even noble-metal containing catalysts.

The ethene selectivity is also increased considerably relative to the Co_3O_4-catalysed transformation (about 3%) for $Ni_{0.1}Co_{2.9}O_4$ (52%) and $FeCo_2O_4$ (18%). It should be noticed that the selectivity value is important for the iron-containing compound since the formation rate is practically zero for the other compound.

XRD analysis of the spent catalysts showed that All nickel-, manganese- and the iron-containing spinel catalysts lost their structure after the CO_2 hydrogenation reaction (Fig. S5). The new reflections at around ~42–45° and ~51–53° 2θ values indicate the reduction of the metals in the structure. The peaks are assigned to reflections from the (1 1 1) and (2 0 0) plates of the face centred cubic crystal structure [40]. In the case of the nickel-containing systems, alloy formation can be assumed, whereas the double peaks in the case of the $Fe_xCo_{3-x}O_4$ cobaltite prove that iron and cobalt metal crystallized in a pseudo-cubic cell [41]. The used structure of manganese-containing systems could be separated to well-characterised part as fcc MnO and fcc metallic Co.

H_2-TPR experiments (*detailed explanation in the supporting information, Fig. S6.*) showed that the reducibility of the pure Co_3O_4 spinel structure is drastically changed when other metals were incorporated into the structure. Also, the concentration of the used metals has a great influence on the structure modification under H_2 atmosphere. These variety of reductions under the reaction conditions has a great influence on the catalytic activity and special selectivity.

As the $MnCo_2O_4$ structure-based catalysts showed dramatically high performance as well as high methane selectivity even at high temperature this structure was examined in details as reported in the following sections to understand their catalytic activity on the molecular level.

4. In-situ investigation of the $MnCo_2O_4$ structure

4.1. Near ambient pressure XPS measurements

$MnCo_2O_4$ spinel structures were examined in detail for molecular level understanding of the high activity and selectivity towards methane of such catalysts even at high temperature. As the chemical state of the surface layer of a catalyst has a decisive role in the reactivity, the $MnCo_2O_4$ sample was characterized under operando conditions (during the catalytic reaction) by NAP-XPS in order to reveal the oxidation state of the topmost few nm (Fig. 5). The assignment of the observed peaks was performed based on previous studies summarized here.

For cobalt, the 2p region was collected. It is known from literature that metallic cobalt is characterized by asymmetric $2p_{3/2}$ and $2p_{1/2}$ peaks at 777.9–778.5 eV, and at 792.95–793.5 eV, respectively, with a peak separation of 15.05 eV. CoO is characterized by Co $2p_{3/2}$ and $2p_{1/2}$ main peaks at 780–781 eV and 795.5–796.5, respectively, with a peak separation of 15.5–15.9 eV. Strong shake up satellites are also present in the Co 2p region of CoO at ~786.5 eV and at ~802 eV. For Co_3O_4, which contains both Co^{3+} and Co^{2+} ions, the main $2p_{3/2}$ and $2p_{1/2}$ peaks can be found at slightly smaller binding energies compared to CoO (at ~779.6 eV,
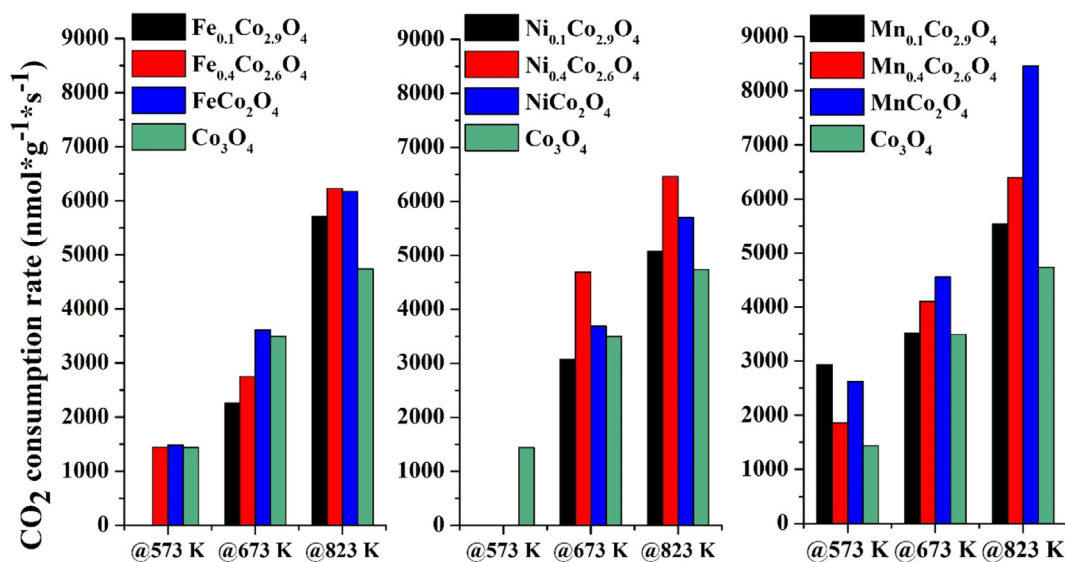
Fig. 3. Consumption rates of CO_2 hydrogenation over $Mn_xCo_{3-x}O_4$, $Ni_xCo_{3-x}O_4$ and $Fe_xCo_{3-x}O_4$ cobaltites at 573 – 823 K.
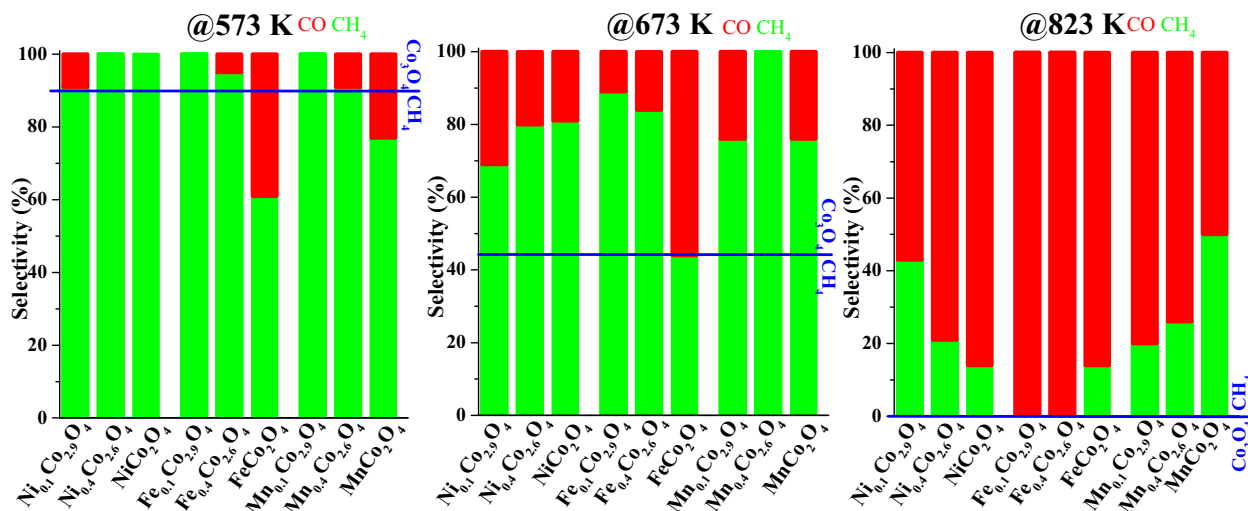

Fig. 4. Selectivity of CO_2 hydrogenation over cobaltites at different temperatures. (Green: methane; red: CO.) (The black horizontal lines show the selectivity of the pure Co_3O_4 spinel catalysts towards methane).

and ~794.6 eV, respectively), and the satellite structure is much weaker, but broadened up to higher binding energies. The spin orbit split for Co_3O_4 is relatively small (~15.0 eV) [42–45].

As regards manganese, previous studies revealed that metallic manganese gives rise to $2p_{3/2}$ and $2p_{1/2}$ peaks at 638.8 – 639.2 eV, and 650.0 – 650.2 eV, respectively with a spin orbit split of 11.2 eV [46–48]. The Mn 2p region of MnO is characterized by $2p_{3/2}$ and $2p_{1/2}$ peaks at 640.6–641.7 eV, and 652.2–653.3 eV, respectively. Importantly, a strong shake-up satellite is also present at the high binding energy side of both peaks at a distance of ~5.7 eV [46,49,50]. The binding energy of the Mn $2p_{3/2}$ peak for Mn_2O_3 is higher by ~0.9 eV (641.9 eV), and the shake-up satellites are more separated from the main peaks (by ~10.5 eV) [46]. Since the satellite of the $2p_{3/2}$ peak overlaps with the $2p_{1/2}$ peak, the satellite of the $2p_{1/2}$ peak is much easier to observe. For MnO_2 the $2p_{3/2}$ and $2p_{1/2}$ peaks were found at 641.9–642.4 and 653.7–654.1 eV, respectively. The shake-up satellite of the $2p_{1/2}$ peak was found at a distance of 11.8 eV. The spin orbit split for the oxidized forms is 11.6 – 11.8 eV [51–53]. While metallic Mn

can be easily distinguished from Mn oxides based on the binding energies, the difference between chemical shifts for various oxides is not particularly large. Therefore, investigation of the satellite structure is crucial. In order to corroborate analysis, the Mn 3p region was also collected. The (typically) unresolved Mn 3p peak can be found at 48.3 eV, 49.3 eV, 49.7 eV, and 50.4 eV for MnO, Mn_3O_4, Mn_2O_3 and MnO_2, respectively, with an asymmetric line shape [53].

In our case, first a spectrum was registered after the oxidation and reduction pretreatment, performed at 573 K. The spectrum was collected in 1 mbar of H_2 (at 573 K) in order to avoid reoxidation due to background gases (Fig. 5 top curves). Considering peak positions, satellite structure and doublet separation, the Co 2p region measured after oxidation and reduction is dominated by Co^{2+} with a minor contribution of metallic Co (Fig. 5/**A**). Although we cannot completely rule out the presence of Co^{3+} traces, based on the Co 2p region it is safe to conclude that the surface layer of the $MnCo_2O_4$ spinel essentially decomposed to some Co^{2+} containing form, and Co metal. Peak fitting yielded a Co^0/Co^{2+} atomic ratio
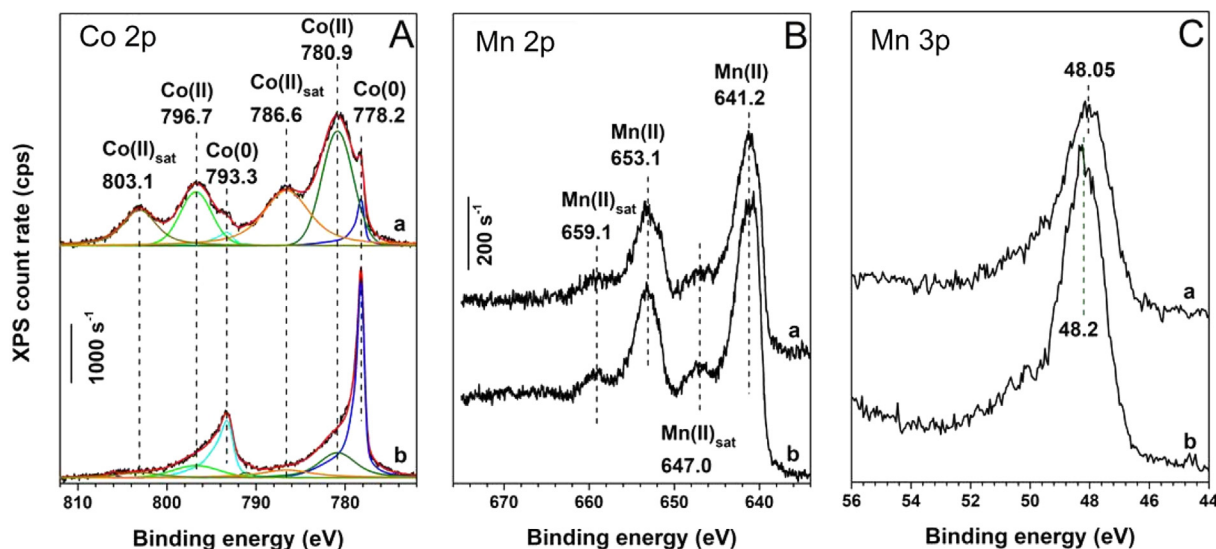
Fig. 5. (a) XPS spectra of $MnCo_2O_4$ collected after oxidation and reduction at 573 K (recorded at 573 K in 1 mbar H_2); (b) XPS spectra collected in 2.5 mbar $CO_2 + H_2$ (1:4) at 743 K. **A:** Co 2p region, Shirley baselines were subtracted. **B:** Mn 2p region; **C:** Mn 3p region.

of 0.10, not considering possibly different concentration gradients along the surface normal. The metallic peak shape and peak position were taken from a reference sample containing metallic cobalt and almost no O, and was kept fixed during fitting. For the Co^{2+} main peaks and satellites, Voigt line shapes were used. A Shirley baseline was subtracted. The Mn $2p_{3/2}$ and Mn $2p_{1/2}$ peaks were observed at 641.2 eV, and 653.1 eV, respectively, while the corresponding shake up satellites appeared at 647.0 eV, and 659.1 eV. Based on the main peak positions and the distance of satellites from main peaks, it is safe to conclude that Mn can be found predominantly in Mn^{2+} oxidation state after pretreatment. The binding energy observed in the Mn 3p region (48.05 eV) is also compatible with the assignment to Mn^{2+}. Contrary to Co, the amount of metallic Mn (with expected peak positions at 639.0 eV, and 650.1 eV) is obviously negligible. Using Shirley baselines, Scofield cross sections and inelastic mean free path (imfp) values of Seah and Dench, assuming homogeneous elemental distribution, the surface composition was estimated to be $MnCo_4O_5$, after subtracting metallic Co contribution. This is in accordance with the observed oxidation states (Mn^{2+} and Co^{2+}), but clearly indicates the enrichment of the surface region in Co, even if metallic Co is not considered.

The chemical state of the surface during catalytic reaction was analysed collecting a spectrum in the reaction mixture, 2.5 mbar $CO_2 + H_2$ (1:4), at 743 K, started 30 min after gas admission. Pronounced changes were observed in the Co 2p region, as shown by trace **b** in Fig. 5/**A**. The metallic Co contribution was greatly enhanced, while the Co^{2+} features decreased a lot. Peak fitting yielded a Co^0/Co^{2+} atomic ratio of 1.54. On the other hand, only minor changes were observed in the peak shapes/positions in the Mn 2p and Mn 3p regions. The slight shift of the Mn 3p peak up to higher binding energies suggests some oxidation of manganese, but the satellite structure in the Mn 2p region clearly indicates the dominance of Mn^{2+}. Although the gas pressure during spectrum collection was higher than that applied after pretreatment, the Mn peaks significantly increased. The overall Mn 2p/Co 2p area ratio increased by 88% as an effect of reaction. In the same way as it was done for the state after reduction, the stoichiometry of the oxidized part was deduced also under reaction conditions using XPS peak areas. First the metallic Co 2p part was subtracted from the Co 2p area. The mean oxide stoichiometry was obtained to be $Mn_{3.3}Co_{2.0}O_{4.7}$, in reasonable agreement with the observed

oxidation states. It should be noted that possible concentration gradients were neglected, and it is not possible to discriminate based on XPS data, whether Mn and Co form a mixed oxide or separate phases. Anyhow, we feel safe to conclude that the oxidized part of the surface turned to be enriched in manganese during reaction conditions with a structure of $Mn_{3.3}Co_{2.0}O_{4.7}$, while after pretreatment it was enriched in cobalt with a structure of $MnCo_4$-O_5. One reason for it is that the major part of Co was reduced to metallic state, and consequently removed from the oxide.

4.2. TEM and TEM-EDS analysis of used catalysts

Structural and morphological changes of $MnCo_2O_4$ during the catalytic process were investigated by ex situ transmission electron microscopy. The morphological properties were not changed significantly after the treatment in H_2 atmosphere at 573 K (Fig. 6). The aggregation of the particles is also discernible after the reduction while the particle size was also similar (38 ± 11 nm) compared to the non-treated $MnCo_2O_4$ (42 ± 14 nm). After the CO_2 hydrogenation reaction, nanoparticles (metallic Co) were observed covered graphitic and carbon while bigger nanoparticles (MnO) where covered mostly by amorphous carbon due to the coke formation after the CO_2 hydrogenation reaction.

In the case of the as-synthetized $MnCo_2O_4$, the measured d-spacing of 0.472 and 0.290 nm can be assigned to the (1 1 1) and (2 2 0) planes of the $MnCo_2O_4$ phase which are in good agreement with the XRD results (PDF#23-1237).

This structure was modified by the treatment in hydrogen atmosphere. Insets of Fig. 6/e. show the presence of 0.257, 0.204 and 0.213 nm d-spacings that correspond to the (1 1 1) crystal plane of cubic MnO (PDF# 75-0257), the (1 1 1) of Co (PDF# 15-0806) and (2 0 0) planes of CoO phase (PDF#75-0533). This agrees well with the results of near ambient pressure XPS measurements that showed the presence of MnO, metallic cobalt and CoO during the treatment of the catalyst in hydrogen atmosphere. Furthermore, a presence of $MnCo_2O_4$ was also discernible due to the 0.472 nm lattice spacing of its (1 1 1) plane (PDF#23-1237). These results confirm the transformation of the original spinel structure to a mixed-oxide phase.

HRTEM and STEM-EDS studies showed that mostly smaller Co nanoparticles and bigger MnO nanoparticles were formed after
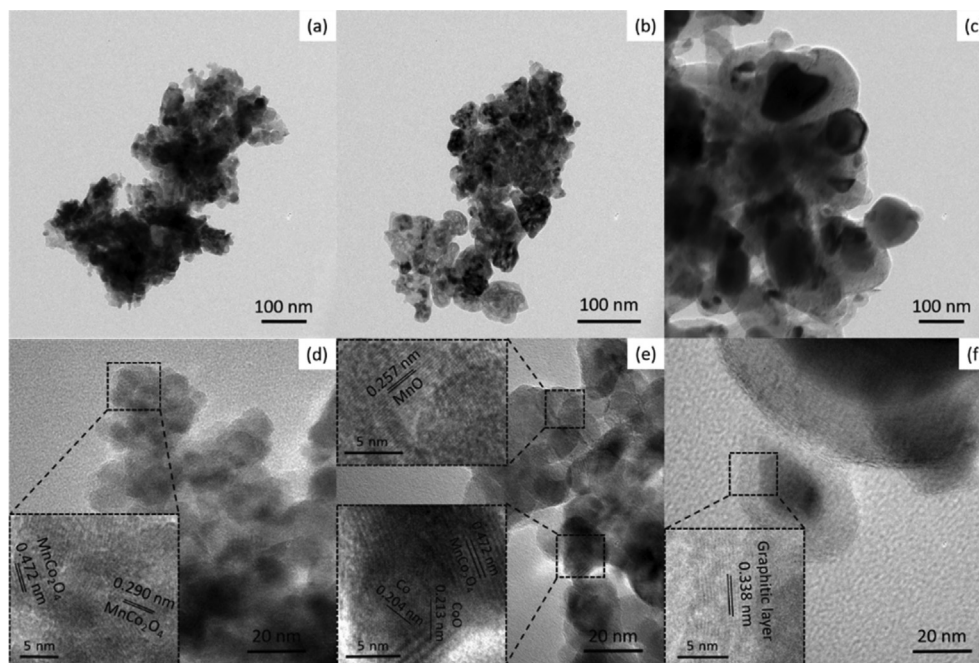
Fig. 6. TEM images of MnCo$_2$O$_4$ (a, d) as-synthetized, (b, e) after the reduction step (300 °C O$_2$ for 1 h followed by 300 °C H$_2$, 1 h) and (c, f) after CO$_2$ hydrogenation 523 – 823 K.

the catalytic reduction of CO$_2$ (Figs. 6c, S8, S9). On the surface of the Co and MnO nanoparticles, hexagonal graphitic as well as amorphous carbon was formed, respectively. The lattice spacing of the covering layer in the Co nanoparticles was determined to be 0.338 nm (inset of Fig. 6f.) which corresponds to the (0 0 2) crystal plane of graphite phase (PDF#01-0640). It is interesting to note, that ~10–15 nm of structured graphitic cover was formed around the Co nanoparticles, however just 2–5 nm thick amorphous carbon layer was determined around Co/MnO catalyst part and pure MnO-based support (Fig. S8).

SAED techniques integrated with the usage of the ProcessDiffraction software showed that after the reaction metallic Cobalt as well as MnO phase was formed (Fig. S7).

Mn as well as Co cation distribution is homogeneous in case of the as-prepared catalyst evidenced by ex-situ HAADF-EDX (Fig. S8). Upon applying the heat treatment, a homogeneous mixed oxide system could be seen. Mostly without accumulation of any of the metals, but in some of the grains the Co and Mn segregation can be shown (Fig. S9). However, in the case of the used catalyst, separated cobalt and manganese-based nanostructures were formed, where some of the smaller Co-based structures are connected to the bigger Mn-based species, and also some of the Co grains are segregated from the Mn-based grains. Based on TEM, XRD and NAP-XPS it is obvious that Co-metal nanoparticles were formed and some of them were embedded into the structure of MnO species to form the special catalyst having outstanding performance in CO$_2$ hydrogenation towards methane (Fig. 7).

4.3. Mechanism and moderating effects

For catalytic reactions, the exploration of surface species formed during the catalytic processes plays a decisive role in the understanding of the reaction mechanism. In our experiments DRIFT spectra were taken at increasing reaction temperatures (linear heating; 20 K/min) in the presence of CO$_2$:H$_2$ mixture with a 1:4 vol ratio using the spectra of spinels without reactants as a background. In this way we could detect the adsorbed species on the surface and the gas phase products formed during the catalytic

reaction [6,12,54,55]. The assignment of IR bands and the detailed description is based on the vibrational fingerprints of relevant surface species, which were reported in the previous publications.

MnCo$_2$O$_4$ spinel structures were examined in detail for understanding of the high activity and selectivity towards methane of such catalysts even at high temperature. The formation of vibrationally or electronically activated CO$_2$ (denoted as CO$_2^{*-}$) is generally accepted in CO$_2$ transformation reactions [56–58]. The activated surface species reacts further in different ways according to the oxidation states of active sites of the catalysts.

$$CO_{2(g)} \rightarrow CO_{2(a)}{}^* \qquad (1)$$

When CO$_2$:H$_2$ mixture was introduced to the spinel catalysts a strong band appeared at 1623 cm^{-1} and some weaker ones at 1417 and 1220 cm^{-1} at 300 K, as represented in Fig. 8 for MnCo$_2$-O$_4$. These bands correspond to the bicarbonate (HCO$_3^-$) species and can be assigned to ν_2(OCO)$_a$, ν_3(OCO)$_s$ and δ_4(COH), respectively [12,59,54]. Different kind of carbonates can be also identified at ~1515, ~1478, 1417, 1371 and 1025–1062 cm^{-1} [55]. Overtones of gas phase CO$_2$ and OH bond modes appeared between 3600 and 3727 cm^{-1} (not shown). Bicarbonate structures may be formed via coordination of a bent CO$_2^{\delta-}$ towards an oxygen atom in the presence of hydrogen [12,60].

$$CO_{2(a)}{}^* + OH_{(a)} \rightarrow HCO_3{}^-{}_{(a)} \qquad (2)$$

When the sample is heated to 473 K, the intensity of bicarbonate peaks significantly decreased. The bands due to monodentate (and polydentate) carbonates remained at 1501–1515, 1371 and 1062–1025 cm^{-1}, which are presented up to high temperatures. Even at low temperature, a shoulder (later peak) at 1533 and 1344 cm^{-1} started developing due to formate, attributable to ν_a(-OCO) and ν_S(OCO) modes in bidentate structure [15,60,61,62]. From 473 to 573 K a band also appeared at 1585 cm^{-1}, its intensity increased with rising temperature and shifted to 1578 cm^{-1} (Fig. 8). This band corresponds to bridge bonded formate [14,55,63]. As it can be seen also in the figures, C-H stretch for formate at 2830 cm^{-1} is also detectable with the combination mode
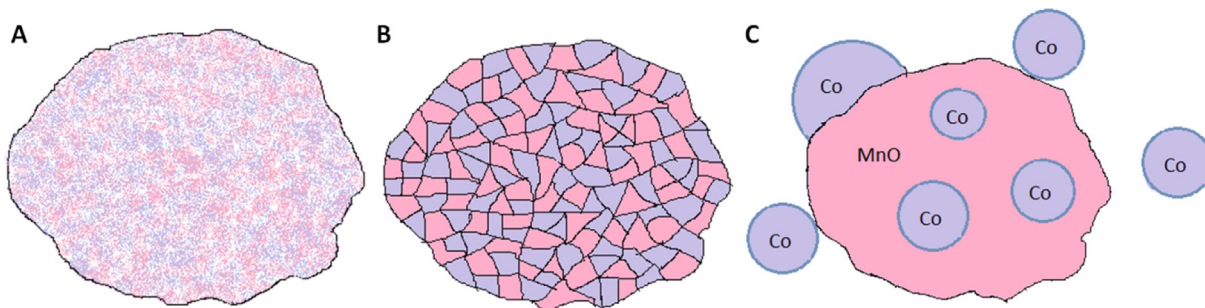
Fig. 7. Schematic view of the transformation of $MnCo_2O_4$ spinel structure (A) to the Co/MnO nanostructure (C) through the mixed oxide phase (B).
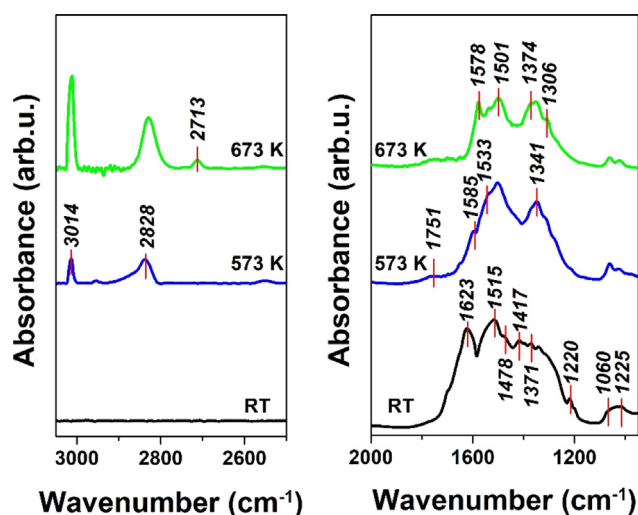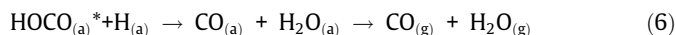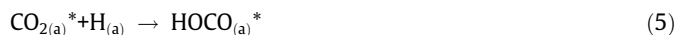

Fig. 8. DRIFTS spectra of $MnCo_2O_4$ structure under reaction conditions (CO_2: H_2 = 1:4, 298–673 K).

at 2712 cm^{-1}. In previous studies [15,60,54] of CO_2 methanation, bicarbonates (HCO_3^-) were found to be intermediate precursor in the formation of formate. It is remarkable that from 573 K IR bands of gas phase methane are detectable on the spectra. A weak vibration is detectable at 1751 cm^{-1} which may attribute to adsorbed formyl (HCO) species [55,64].
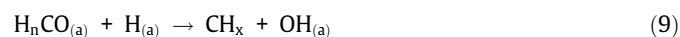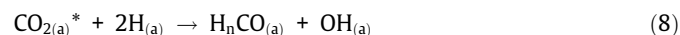
As regard of the reaction mechanism of CO_2 hydrogenation one may argue first that the activated CO_2 is in an anionic or radical form directly dissociates to adsorbed CO with the help of hydrogen [65–67].

$$H_{2(g)} \rightarrow 2H_{(a)} \tag{3}$$

$$CO_{2(g)} \rightarrow CO_{2(a)}{}^* \tag{4}$$

$$CO_{2(a)}{}^* + H_{(a)} \rightarrow HOCO_{(a)}{}^* \tag{5}$$

$$HOCO_{(a)}{}^* + H_{(a)} \rightarrow CO_{(a)} + H_2O_{(a)} \rightarrow CO_{(g)} + H_2O_{(g)} \tag{6}$$

This kind of reverse water–gas shift reaction mechanism was suggested in CO and CO_2 hydrogenation on several supported metals for example on Pt/SiO_2, Pt/TiO_2 [68] and $Pt/Ni/NiO^{15}$. In our case, the CO formation can be explained through this way. The other realistic CO formation route is the decomposition of bidentate formate [15,69,70,71]. We suggest that the most part of the CO produces via the decomposition of formate at low temperature regime:
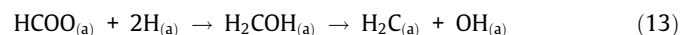
$$HCOO_{(a)} \rightarrow CO_{(a)} + OH_{(a)} \rightarrow CO_{(g)} + H_2O_{(g)} \tag{7}$$
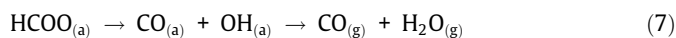
Methane (and/or carbon) formation can be originated from the hydrogen assisted C-O cleavage in CO or H_nCO [65–67].

$$CO_{2(a)}{}^* + 2H_{(a)} \rightarrow H_nCO_{(a)} + OH_{(a)} \tag{8}$$

$$H_nCO_{(a)} + H_{(a)} \rightarrow CH_x + OH_{(a)} \tag{9}$$

$$CH_{3(a)} + H_{(a)} \rightarrow CH_{4(g)} \tag{10}$$

$$CH_{2(a)} + CH_{2(a)} \rightarrow C_2H_{4(g)} \tag{11}$$

$$H_xCO_{(a)} \rightarrow C_{(a)} + OH_{(a)} \tag{12}$$

This reaction route could be valid in certain extent in the present case, especially where metallic particles form during the pre-treatment or under catalytic reaction (see XRD, TPR and XPS sections). As tentatively adsorbed formyl was identified at 1751 cm^{-1} in our DRIFTS experiments, therefore we suggest that a fraction of reaction may proceed partially according to the above mentioned reaction mechanisms.

It is revealed from catalytic measurements, that methane formation is dominant at higher temperature and gas phase methane vibrations (DRIFTS) appeared also with high intensity from 573 K, and the intensity of the IR band due to C-H stretch of formate also increased significantly from 573 K to 673 K. (Fig. 8). For further analysis, the DRIFT spectrum obtained at 673 K is deconvoluted and displayed in Fig. S9.

At high reaction temperature, Co(0) and Mn(II) states are dominant as evidenced by NAP-XPS (Fig. 5). At the same time, a new formate group could be detected at 1585–1578 cm^{-1} which can be attributed to ν_a(OCO) mode in bridge bonded formate [14,55]. We believe that catalytic data and spectroscopic observation are correlated, namely the bridge bonded formate located at Co/Mn^{2+} interface environment responsible mainly for methane formation. The metallic Co plays an important role in the dissociation of the hydrogen and in the activation of the CO_2. On the other hand, the Mn^{2+} at the interface may have high ability to bond the formate (appeared at 1578–1585 cm^{-1}) and the metallic Co could deliver sufficient amount of hot hydrogen atoms, which could rapture the C-O bond in formate species. These features may stress that bridge bonded formate existed at high temperature at the interface is a key intermediate in high temperature methane formation on $MnCo_2O_4$:

$$HCOO_{(a)} + 2H_{(a)} \rightarrow H_2COH_{(a)} \rightarrow H_2C_{(a)} + OH_{(a)} \tag{13}$$

$$H_2C_{(a)} + 2H_{(a)} \rightarrow CH_{4(g)} \tag{14}$$

As the band for gas phase methane increased somewhat higher extent (1.6) than that of formate, we suggest that beside the formate-route, the methane formation proceeds partially via hydrogenation of formyl species predominantly on bare metallic Co particles (steps 9, 10), too.
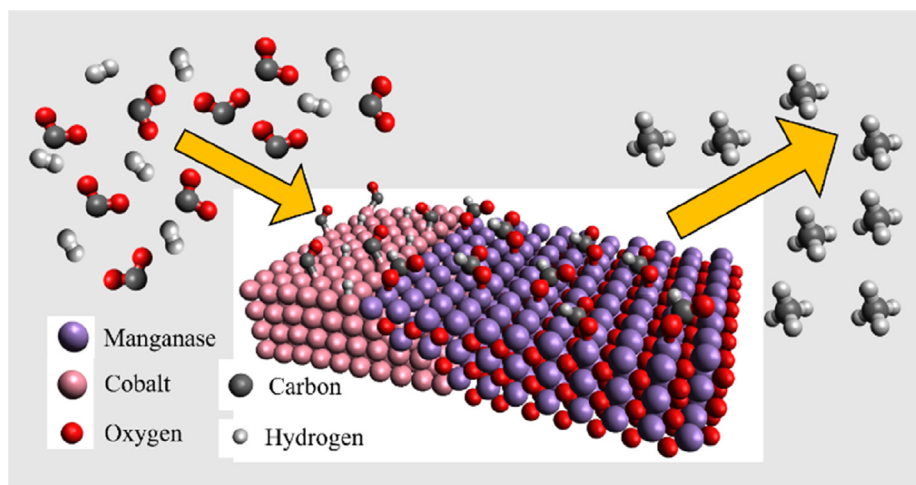
Fig. 9. Schematic of the proposed mechanism of CO_2 hydrogenation towards CH_4 on the Co/MnO interface formed under reaction conditions in the case of the $MnCo_2O_4$ spinel catalysts.

Coke formation detected by TEM can be described by the subsequent dehydrogenation of $CH_{2(a)}$ on metallic Co which is a well-known process on this metal [72]. The hydrogen formed in dehydrogenation desorbs molecularly at high reaction temperature:

$$H_2C_{(a)} \rightarrow C_{(a)} + H_{2(g)} \tag{15}$$

In Summary, from the NAP-XPS, XRD, STEM, HAADF-EDX measurements we can conclude that during the pretreatment as well as the CO_2 hydrogenation a metallic Co/Mn(II)O nanoparticle structure forms from the initial $MnCo_2O_4$ spinel structure (Fig. 9). The oxidized part of the surface turned to be enriched in manganese during reaction conditions, while after pretreatment it was enriched in cobalt. One reason for it is that the major part of Co was reduced to metallic state, and consequently removed from the oxide. We believe that this special Co/MnO interface play an important role in the high activity and outstanding CH_4 selectivity even at elevated temperatures.

On the other hand, DRIFTS studies showed that the mechanism of the CO_2 hydrogenation follows the 'formate route' instead of the 'perturbated CO' pathway usually observed on metal/oxide interfaces. The formed Co/MnO interface are responsible for the activation of the formate intermediers on the surface, which in turn produces methane even at high temperatures where usually the CO formation is favourable evidenced by the thermodynamics of the CO_2 hydrogenation reaction.

5. Conclusions

In this study, $Mn_xCo_{3-x}O_4$, $Ni_xCo_{3-x}O_4$ and $Fe_xCo_{3-x}O_4$ cobaltite-based spinel structures were prepared. Mixed spinel as well as inverse spinel structures were formed evidenced by XRD and Raman techniques. All the spinels were tested in CO_2 hydrogenation reaction at ambient pressure in the range of 573–823 K in a gas phase flow reactor. $MnCo_2O_4$ structure had the highest activity among these catalysts ($5100 \ nmol*g^{-1}*s^{-1}$). Furthermore, this activity of the manganese-based catalysts is superior to those reported in the literature.

The pure cobaltite had 92% selectivity for methane at 573 K. However, 60% methane selectivity was detected at 673 K and only CO was formed at 823 K. On the contrary, both the manganese-, and iron-containing systems demonstrated 100% methane selectivity at 573 K, moreover, up to 90% methane selectivity was observed in case of $Fe_{0.1}Co_{2.9}O_4$ even at 673 K. Furthermore, all modified spinels produced measurable amounts of methane at

823 K. The $MnCo_2O_4$ structure exhibited ~50% methane selectivity at ambient pressure and at 823 K, which is unique compared to the literature. This activity and selectivity is slowly decreased after >3 h run and the catalyst can be reactivated by thermal treatments several times.

In-situ as well as ex-situ techniques (XRD, TEM, HAADF-EDX, NAP-XPS, DRIFTS) helped us to understand the structure of the $MnCo_2O_4$ as well as the reaction mechanism under reaction conditions on the molecular level. Hence, during the CO_2 hydrogenation reaction a metallic Co/Mn(II)O nanoparticle structure forms from the initial $MnCo_2O_4$ spinel structure. DRIFTS studies showed that the mechanism of the CO_2 hydrogenation follows the 'formate route' instead of the 'perturbated CO' pathway usually observed on metal/oxide interfaces. We believe that the formed Co/MnO interface are responsible for the methane production even at high temperatures. In the future, we will produce other Co/MnO_x structures towards high activity and selectivity usage.

Declaration of Competing Interest

The authors declare that they have no known competing financial interests or personal relationships that could have appeared to influence the work reported in this paper.

Acknowledgement

Appendix A. Supplementary material

Supplementary data to this article can be found online at https://doi.org/10.1016/j.jcat.2020.03.028.

References

[1] N.S. Lewis, D.G. Nocera, Powering the planet: Chemical challenges in solar energy utilization, Proc. Natl. Acad. Sci. 103 (2006) 15729–15735.

[2] G.A. Olah, A. Goeppert, G.K.S. Prakash, Beyond Oil and Gas: The Methanol Economy: Second Edition, Beyond Oil Gas Methanol Econ. Second Ed. 1–334 (2009), https://doi.org/10.1002/9783527627806.

[3] C.-S. Li et al., High-performance hybrid oxide catalyst of manganese and cobalt for low-pressure methanol synthesis, Nat. Commun. 6 (2015) 6538.

[4] P. Gao et al., Direct conversion of CO2 into liquid fuels with high selectivity over a bifunctional catalyst, Nat. Chem. 9 (2017) 1019–1024.

[5] J. Wei et al., Directly converting CO2 into a gasoline fuel, Nat. Commun. 8 (2017) 15174.

[6] Z. He et al., Synthesis of liquid fuel via direct hydrogenation of CO2, Proc. Natl. Acad. Sci. U. S. A. 116 (2019) 12654–12659.

[7] C. Xie et al., Tandem Catalysis for CO2 Hydrogenation to C2–C4 Hydrocarbons, Nano Lett. 17 (2017) 3798–3802.

[8] A. Sápi et al., Noble-metal-free and Pt nanoparticles-loaded, mesoporous oxides as efficient catalysts for CO 2 hydrogenation and dry reforming with methane, J. CO2 Util. 32 (2019) 106–118.

[9] X. Wang, H. Shi, J. Szanyi, Controlling selectivities in CO2 reduction through mechanistic understanding, Nat. Commun. 8 (2017) 513.

[10] F. Wang et al., Active Site Dependent Reaction Mechanism over Ru/CeO2 Catalyst toward CO2 Methanation, J. Am. Chem. Soc. 138 (2016) 6298–6305.

[11] W. Taifan, J.F. Boily, J. Baltrusaitis, Surface chemistry of carbon dioxide revisited, Surf. Sci. Rep. 71 (2016) 595–671.

[12] K. Jalama, Carbon dioxide hydrogenation over nickel-, ruthenium-, and copper-based catalysts: Review of kinetics and mechanism, Catal. Rev. 59 (2017) 95–164.

[13] C. Vogt et al., Unravelling structure sensitivity in CO2 hydrogenation over nickel, Nat. Catal. 1 (2018) 127–134.

[14] K. Zhao, L. Wang, M. Calizzi, E. Moioli, A. Züttel, In Situ Control of the Adsorption Species in CO2 Hydrogenation: Determination of Intermediates and Byproducts, J. Phys. Chem. C 122 (2018) 20888–20893.

[15] A. Sápi et al., In Situ DRIFTS and NAP-XPS Exploration of the Complexity of CO2 Hydrogenation over Size-Controlled Pt Nanoparticles Supported on Mesoporous NiO, J. Phys. Chem. C 122 (2018) 5553–5565.

[16] P. Frontera, A. Macario, M. Ferraro, P. Antonucci, Supported catalysts for CO2 methanation: a review, Catalysts 7 (2017) 59.

[17] T. Franken, J. Terreni, A. Borgschulte, A. Heel, Solid solutions in reductive environment – A case study on improved CO2 hydrogenation to methane on cobalt based catalysts derived from ternary mixed metal oxides by modified reducibility, J. Catal. 382 (2020) 385–394.

[18] J. Park, E.W. Mcfarland, A highly dispersed Pd – Mg / SiO2 catalyst active for methanation of CO2, J. Catal. 266 (2009) 92–97.

[19] J. Kielhorn, C. Melber, D. Keller, I. Mangelsdorf, Palladium - A review of exposure and effects to human health, Int. J. Hyg. Environ. Health 205 (2002) 417–432.

[20] M. Haruta et al., Low-temperature oxidation of CO over gold supported on TiO2, α-Fe2O3, and Co3O4, J. Catal. 144 (1993) 175–192.

[21] S. Velu, K. Suzuki, C.S. Gopinath, Photoemission and in Situ XRD Investigations on CuCoZnAl-Mixed Metal Oxide Catalysts for the Oxidative Steam Reforming of Methanol, J. Phys. Chem. B 106 (2002) 12737–12746.

[22] G. Zhan, C.C. Yec, H.C. Zeng, Mesoporous Bubble-like Manganese Silicate as a Versatile Platform for Design and Synthesis of Nanostructured Catalysts, Chem. – A Eur. J. 21 (2015) 1882–1887.

[23] R. Nafria et al., Co-Cu Nanoparticles: Synthesis by Galvanic Replacement and Phase Rearrangement during Catalytic Activation, Langmuir 32 (2016) 2267–2276.

[24] R. Langer et al., Low-Pressure Hydrogenation of Carbon Dioxide Catalyzed by an Iron Pincer Complex Exhibiting Noble Metal Activity, Angew. Chemie Int. Ed. 50 (2011) 9948–9952.

[25] H. Ando et al., Hydrocarbon synthesis from CO2 over Fe-Cu catalysts, Catal. Today 45 (1998) 229–234.

[26] N. Wang, W. Chu, T. Zhang, X.S. Zhao, Manganese promoting effects on the Co-Ce-Zr-Ox nano catalysts for methane dry reforming with carbon dioxide to hydrogen and carbon monoxide, Chem. Eng. J. 170 (2011) 457–463.

[27] G. Centi, E. Quadrelli, S. Perathoner, Catalysis for CO2 conversion: A key technology for rapid introduction of renewable energy in the value chain of chemical industries, Energy Environ. Sci. 6 (2013) 1711–1731.

[28] N. Yamamoto, S. Higashi, S. Kawano, N. Achiwa, Preparation of MnCo2O4 by a wet method and its metal ion distribution, J. Mater. Sci. Lett. 2 (1983) 525–526.

[29] J.L. Lábár, Electron Diffraction Based Analysis of Phase Fractions and Texture in Nanocrystalline Thin Films. Part I : Principles, Microsc. Microanal. 14 (2008) 287–295.

[30] J.L. Lábár, Electron Diffraction Based Analysis of Phase Fractions and Texture in Nanocrystalline Thin Films. Part II: Implementation, Microsc. Microanal. 15 (2009) 20–29.

[31] J.L. Lábár et al., Electron Diffraction Based Analysis of Phase Fractions and Texture in Nanocrystalline Thin Films, Part III : Application Examples, Microsc. Microanal. 18 (2012) 406–420.

[32] X.-C. Dong et al., 3D Graphene-Cobalt Oxide Electrode for High-Performance Supercapacitor and Enzymeless Glucose Detection, ACS Nano 6 (2012) 3206–3213.

[33] J. Kreisel, G. Lucazeau, H. Vincent, Raman Spectra and Vibrational Analysis of BaFe 12 O 19 Hexagonal Ferrite, J. Solid State Chem. (1998), https://doi.org/10.1006/jssc.1997.7737.

[34] J. Jacob, M. Abdul Khadar, Investigation of Mixed Spinel Structure of Nanostructured Nickel Ferrite, J. Appl. Phys. 107 (2010) 114310.

[35] J. Wu et al., A highly active oxygen evolution electrocatalyst: Ultrathin CoNi double hydroxide/CoO nanosheets synthesized via interface-directed assembly, Nano Res. 9 (2016) 713–725.

[36] X.F. Lu et al., Bimetal-Organic Framework Derived CoFe2O4/C Porous Hybrid Nanorod Arrays as High-Performance Electrocatalysts for Oxygen Evolution Reaction, Adv. Mater. 29 (2017).

[37] S. Xu et al., Engineered morphologies of layered double hydroxide nanoarchitectured shell microspheres and their calcined products, Chem. Eng. Sci. 66 (2011) 2157–2163.

[38] P. Saikia, J. Saikia, S. Sarmah, N.B. Allou, R.L. Goswamee, Mesoporous oxidic holey nanosheets from Zn-Cr LDH synthesized by soft chemical etching of Cr3+ and its application as CO2 hydrogenation catalyst, J. CO2 Util. 21 (2017) 40–51.

[39] N. Bette, J. Thielemann, M. Schreiner, F. Mertens, Methanation of CO2 over a (Mg, Al)Ox Supported Nickel Catalyst Derived from a (Ni, Mg, Al)-Hydrotalcite-like Precursor, ChemCatChem 8 (2016) 2903–2906.

[40] Z. Wu, H. Bei, F. Otto, G.M. Pharr, E.P. George, Recovery, recrystallization, grain growth and phase stability of a family of FCC-structured multi-component equiatomic solid solution alloys, Intermetallics 46 (2014) 131–140.

[41] H. Li et al., Transmission electron microscopy and x-ray structural investigation of La0.7Ca0.3MnO3 thin films, J. Mater. Res. 13 (1998) 2161–2169.

[42] T.J. Chuang, C.R. Brundle, D.W. Rice, Interpretation of the x-ray photoemission spectra of cobalt oxides and cobalt oxide surfaces, Surf. Sci. 59 (1976) 413–429.

[43] C.D. Wagner, W.M. Riggs, L.E. Davis, J. Moulder, Handbook of X-Ray Photoelectron Spectroscopy, Perkin-Elmer Corporation, Eden Praire, 1979.

[44] S.S.Y. Lin, D.H. Kim, M.H. Engelhard, S.Y. Ha, Water-induced formation of cobalt oxides over supported cobalt/ceria-zirconia catalysts under ethanol-steam conditions, J. Catal. 273 (2010) 229–235.

[45] L. Óvári et al., Near ambient pressure XPS investigation of the interaction of ethanol with Co/CeO2(1 1 1), J. Catal. 307 (2013) 132–139.

[46] V. Di Castro, G. Polzonetti, XPS study of MnO oxidation, J. Electron Spectros. Relat. Phenomena 48 (1989) 117–123.

[47] A. Chourasia, D. R. Chopra, Elemental Manganese Studied by X-ray Photoemission Spectroscopy Using Mg and Zr Radiations, Surf. Sci. Spectra 3 (1994).

[48] C.J. Jenks, S.-L. Chang, J.W. Anderegg, P.A. Thiel, D.W. Lynch, Photoelectron spectra of an Al70Pd21Mn9 quasicrystal and the cubic alloy Al60Pd25Mn15, Phys. Rev. B 54 (1996) 6301–6306.

[49] M. Oku, K. Hirokawa, S. Ikeda, X-ray photoelectron spectroscopy of manganese-oxygen systems, J. Electron Spectros. Relat. Phenomena 7 (1975) 465–473.

[50] B.R. Strohmeier, D.M. Hercules, Surface spectroscopic characterization of manganese/aluminum oxide catalysts, J. Phys. Chem. 88 (1984) 4922–4929.

[51] M.A. Stranick, MnO2 by XPS, Surf. Sci. Spectra 6 (1999) 31–38.

[52] M.C. Militello, S.W. Gaarenstroom, Manganese Dioxide (MnO2) by XPS, Surf. Sci. Spectra 8 (2001) 200–206.

[53] G.C. Allen, S.J. Harris, J.A. Jutson, J.M. Dyke, A study of a number of mixed transition metal oxide spinels using X-ray photoelectron spectroscopy, Appl. Surf. Sci. 37 (1989) 111–134.

[54] X. Wang, Y. Hong, H. Shi, J. Szanyi, Kinetic modeling and transient DRIFTS – MS studies of CO 2 methanation over Ru / Al 2 O 3 catalysts, J. Catal. 343 (2016) 185–195.

[55] Y. Guo et al., Low-Temperature CO2 Methanation over CeO2-Supported Ru Single Atoms, Nanoclusters, and Nanoparticles Competitively Tuned by Strong Metal-Support Interactions and H-Spillover Effect, ACS Catal. 8 (2018) 6203–6215.

[56] F. Solymosi, The bonding, structure and reactions of CO2 adsorbed on clean and promoted metal surfaces, J. Mol. Catal. 65 (1991) 337–358.

[57] J. Kiss, K. Révész, F. Solymosi, Photoelectron spectroscopic studies of the adsorption of CO2 on potassium-promoted Rh(111) surface, Surf. Sci. 207 (1988) 36–54.

[58] H.-J. Freund, M.W. Roberts, Surface chemistry of carbon dioxide, Surf. Sci. Rep. 25 (1996) 225–273.

[59] J. Baltrusaitis, J. Schuttlefield, E. Zeitler, V.H. Grassian, Carbon dioxide adsorption on oxide nanoparticle surfaces, Chem. Eng. J. 170 (2011) 471–481.

[60] X. Wang, H. Shi, J.H. Kwak, J. Szanyi, Mechanism of CO2 Hydrogenation on Pd/Al2O3 Catalysts : Kinetics and Transient DRIFTS-MS Studies, ACS Catal. 5 (2015) 6337–6349.

[61] T. Kecskés, J. Raskó, J. Kiss, FTIR and mass spectrometric studies on the interaction of formaldehyde with TiO 2 supported Pt and Au catalysts, Appl. Catal. A Gen. 273 (2004) 55–62.

[62] J. Raskó, T. Kecskés, J. Kiss, Formaldehyde formation in the interaction of HCOOH with Pt supported on TiO2, J. Catal. 224 (2004) 261–268.

[63] C. Li et al., Adsorption of carbon monoxide and carbon dioxide on cerium oxide studied by Fourier-transform infrared spectroscopy. Part 2. - Formation of formate species on partially reduced CeO2 at room temperature, J. Chem. Soc. Faraday Trans. 1 Phys. Chem. Condens. Phases 85 (1989) 1451–1461.

[64] S. Eckle, H.G. Anfang, R.J. Behm, Reaction intermediates and side products in the methanation of CO and CO2 over supported Ru catalysts in H2-rich reformate gases, J. Phys. Chem. C 115 (2011) 1361–1367.

[65] F. Solymosi, A. Erdöhelyi, T. Bánsági, Methanation of CO2 on supported rhodium catalyst, J. Catal. 68 (1981) 371–382.

[66] Erdohelyi, A., Solymosi F., B. T. Infrared Study of the Surface Interaction between H2, and CO2, over Rhodium on Various Supports. J. Chem. Soc. Farad. Trans. 77 (1981) 2645–2657.

[67] I. A. Fisher, A.T. Bell, A comparative study of CO and CO2 hydrogenation over Rh/SiO2, J. Catal. 162 (1996) 54–65.

[68] S. Kattel, B. Yan, J.G. Chen, P. Liu, CO2 hydrogenation on Pt, Pt/SiO2 and Pt/TiO2: Importance of synergy between Pt and oxide support, J. Catal. 343 (2016) 115–126.

[69] S. Kattel, P. Liu, J.G. Chen, Tuning Selectivity of CO2 Hydrogenation Reactions at the Metal/Oxide Interface, J. Am. Chem. Soc. 139 (2017) 9739–9754.

[70] G. Halasi, G. Schubert, F. Solymosi, Photodecomposition of formic acid on N-doped and metal-promoted TiO 2 production of CO-free H 2, J. Phys. Chem. C 116 (2012) 15396–15405.

[71] B. László et al., Gold Size Effect in the Thermal-Induced Reaction of CO 2 and H 2 on Titania- and Titanate Nanotube-Supported Gold Catalysts, J. Nanosci. Nanotechnol. 19 (2018) 470–477.

[72] F. Steinbach, J. Kiss, R. Krall, Identification and stability of CH3, CH2, and CH species on Co and Ni surfaces, a Pes investigation, Surf. Sci. 157 (1985) 401–412.